Impact of pump pulse duration on modulation instability Kerr frequency combs in fiber Fabry-Pérot resonators

Thomas Bunel, Zoheir Ziani, Matteo Conforti, Julien Lumeau, Antonin Moreau, Arnaud Fernandez, Olivier Llopis, Germain Bourcier, Auro M Perego, Arnaud Mussot

Impact of pump pulse duration on modulation instability Kerr frequency combs in fiber Fabry–Pérot resonators

THOMAS BUNEL[1,*], ZOHEIR ZIANI[1], MATTEO CONFORTI[1], JULIEN LUMEAU[2], ANTONIN MOREAU[2], ARNAUD FERNANDEZ[3], OLIVIER LLOPIS[3], GERMAIN BOURCIER[3,4], AURO M. PEREGO[5], AND ARNAUD MUSSOT[1]

[1] *University of Lille, CNRS, UMR 8523-PhLAM Physique des Lasers Atomes et Molécules, F-59000, Lille, France*
[2] *Aix Marseille Univ, CNRS, Centrale Marseille, Institut Fresnel, Marseille, France*
[3] *LAAS-CNRS, Université de Toulouse, CNRS, 7 avenue de Colonel Roche, 31031 Toulouse, France*
[4] *CNES, 18 Avenue Edouard Belin, F-31401 Toulouse, France*
[5] *Aston Institute of Photonic Technologies, Aston University, Birmingham, B4 7ET, United Kingdom*
[*] *Corresponding author: thomas.bunel@univ-lille.fr*

Compiled April 11, 2024

We report an experimental investigation on the impact of the pump pulse duration on the modulation instability process in fiber Fabry-Pérot resonators. We demonstrate that cross-phase modulation between the forward and the backward waves alters significantly the modulation instability process. By varying the pump pulse duration, we show the modification of the modulation instability threshold and frequency. These experimental observations are in excellent agreement with theoretical predictions.

http://dx.doi.org/10.1364/ao.XX.XXXXXX

Optical frequency combs (OFC) generated in Kerr optical resonators have attracted significant attention over the last decade [1–3]. In particular, OFCs generated by pumping a high-Q microresonator are attractive for a wealth of applications [2, 4]. Fiber Fabry-Pérot (FFP) resonators emerged recently as a promising complement to the well studied ring microresonators [5–10]. FFP resonators combine the advantages of both microresonators and fiber ring cavities, namely, high quality factor, compact design, and the capability to be easily implanted in fibered systems thanks to FC/PC connectors. In these devices, pulsed pumping allows to effectively reduce the average power, to limit the beam fluence sent to the mirrors, and to alleviate the intracavity thermal effect [5–11]. Due to its fundamental role in the nonlinear dynamics of resonators, particularly in the soliton build-up [3, 12], modulation instability (MI) has been deeply investigated in fiber ring resonators [13–17] and microresonators [18–20] but much less in FFP resonators. The dynamics in FFP resonators is much more complicated because backward and forward waves interact within the resonator through cross-phase modulation (XPM). This additional nonlinear phase contribution modifies the dynamics of the MI process in these systems as it was recently theoretically predicted in [21–23]. However, there is a lack of experimental confirmation of these theoretical predictions. In this paper, we experimentally demonstrate the impact of the pump duration on MI in FFP resonators. We show that the threshold and the frequency of the MI sidebands are deeply affected by the pump duration.

We consider a FFP resonator of length L consisting of a Kerr-type nonlinear medium, two identical mirrors, of reflectivity coefficient ρ and transmissivity coefficients θ. We take into account of the overall losses in the reflection coefficients, i.e. $\theta^2+\rho^2 \lesssim 1$, and the cavity losses reads as $\alpha = 1-\rho^2$. As shown in [23], for a FFP cavity pumped with rectangular pulses, of duration δt, input peak power P_{in}, at the repetition rate $1/t_r$ of the cavity, the intracavity peak power P of the circulating forward field in the stationary regime can be written as:

$$P = \frac{\theta^2 P_{in}}{1+\rho^4-2\rho^2\cos(\phi)}, \tag{1}$$

with $\phi = \phi_0 + \phi_{NL}$, ϕ_0 is the cavity linear phase (modulo 2π) and $\phi_{NL} = \gamma(1+\rho^2)(1+\chi G)P$ is the nonlinear phase. $G = 2$ accounts for XPM [21, 22] and $\chi = \delta t/t_R$ is the duty cycle. It is important to note that the effective XPM is reduced by a factor equal to the duty cycle, and therefore depends on the pump duration δt. Through a stability analysis of the stationary solutions, we can derive the parametric gain [23]:

$$g(\omega) = \frac{1}{2L}\ln\max\left|\frac{\Delta(\omega)}{2} \pm \sqrt{\frac{\Delta(\omega)^2}{4}-\rho^4}\right|, \tag{2}$$

$$\Delta(\omega) = \rho^2\cos\phi\left[2\cos(kL)\cos(k_\rho L) - \frac{k^2+k_\rho^2}{kk_\rho}\sin(kL)\sin(k_\rho L)\right]$$
$$-\rho^2\sin\phi\left[\frac{4k^2+\beta_2^2\omega^4}{2\beta_2\omega^2 k}\cos(k_\rho L)\sin(kL) + \frac{4k_\rho^2+\beta_2^2\omega^4}{2\beta_2\omega^2 k_\rho}\cos(kL)\sin(k_\rho L)\right]$$

with $k^2 = \frac{\beta_2\omega^2}{2}\left(\frac{\beta_2\omega^2}{2}+2\gamma P\right)$, and $k_\rho^2 = \frac{\beta_2\omega^2}{2}\left(\frac{\beta_2\omega^2}{2}+2\gamma P\rho^2\right)$. It is worth noting that the parametric gain within a FFP cavity depends on pump duration through the overall phase ϕ. Also, these theoretical developments are valid as long as we are operating in a quasi-CW regime, i.e. when the MI period is well shorter than the pulse duration, which is 2 ps in our configuration.

In Fig. 1, we plot the nonlinear transfer function [Fig. 1(a)] and the cavity response [Fig. 1(b)] for different pump pulse

durations. For pulses much shorter than the cavity round trip time (2 ps vs 637 ps), XPM between forward and backward pulses is negligible and the FFP resonator behaves as a ring resonator [blue lines in Fig. 1(a) and (b)]. By increasing the pulse duration [orange and yellow lines in Fig. 1(a) and (b)], the nonlinear resonance is more tilted [Fig. 1(a)] due to an additional nonlinear phase brought on by XPM. For instance, moving from 480 ps to 160 ps leads to shift the first knee position from 9 W to 14 W for bistable regimes [continuous lines in Fig. 1(b)] and to a significant increase of the stationary power in the monostable regime [dashed lines in Fig. 1(b)].

In the following, we experimentally study an optical cavity in the anomalous dispersion regime, where MI exists in the monostable case above the intracavity power threshold and on the upper branch of the cavity response in bistable zone [14, 23]. A simple but rather accurate estimate of the threshold is $P_{th} = \alpha/(2\gamma L) \approx 64$ W in our case. To quantify the effect of the pump duration on MI in FFP cavities in monostable and bistable regimes, we will follow the evolution of three characteristic points. They are labelled 1, 2 and 3 on the yellow curve in Fig. 1(a): 1 - the MI threshold, 2 - the lower knee of the bistable region, 3 - the upper knee of the bistable region.

The experimental setup is described in Fig. 2(a). We pump a FFP resonator with a square pulse train generated at 1550 nm by a tunable CW laser, and an intensity modulator (IM) which is driven by square electrical pulses from an arbitrary waveform generator (AWG). We finely adjust the bias voltage and the RF amplifier gain to generate flat top optical pulses which duration ranges from 30 to 200 ps [selected examples in Fig. 2(b)]. Thus, we will be able to directly compare our results with theoretical prediction in [23], derived by assuming the cavity is pumped by flat-topped square pulses. Moreover, the clock of the AWG is delivered by a frequency synthesizer allowing us to set the repetition rate very accurately (in the Hz range), in a way that the pulses perfectly overlap in the cavity at each round trip. The pulses are amplified through an EDFA and are launched within the cavity. We use the same cavity as in [9] [insert in Fig. 2(a)] which is made from an optical single-mode fiber (SMF-28) of $L = 6.51$ cm and a group velocity dispersion of $\beta_2 = -22.9$ ps^2 km^{-1} (see Fig. 1 caption for the other parameters). Both fiber ends are mounted in FC/PC connectors and

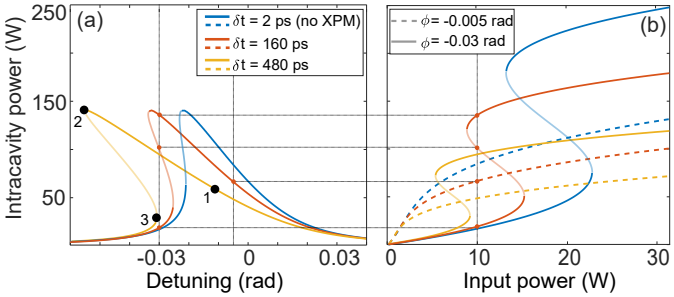

Fig. 1. Numerical results illustrating the transfer function and cavity response, as a function of the pump duration. Cavity parameters: $\rho = 0.9950$; $\theta = 0.0396$; $\alpha = 0.01$; $\gamma = 1.2$ W^{-1} km^{-1}; $\beta_2 = -22.9$ ps^2 km^{-1}; $L = 6.51$ cm; $n = 1.4582$; and $\lambda = 1550$ nm. (a) Intracavity peak power as a function of the phase (fixed input peak power = 10 W). The black numbered points correspond to the characteristic points defined in the main text. (b) Intracavity peak power as a function of the input peak power (fixed phase)

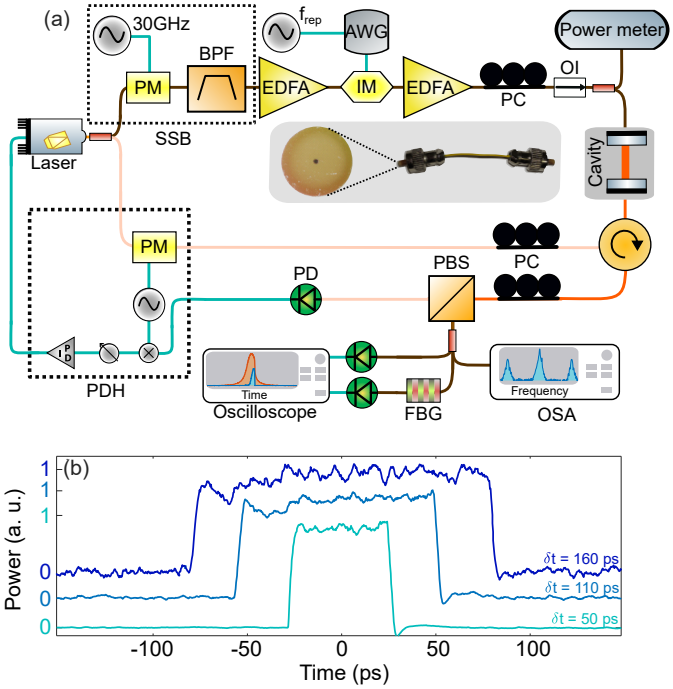

Fig. 2. (a) Experimental setup with a two arms stabilisation system. Brown line: pumping path; beige line: stabilization path. The pumping and stabilization beams are perpendicularly polarized to each other. AWG: Arbitrary Waveform Generator; IM: Intensity Modulator; PM: Phase Modulator; EDFA: Erbium Doped Fiber Amplifier; PC: Polarization Controller; OI: Optical Isolator; FBG: Fiber Bragg Grating; PD: Photo-diode; PDH: Pound-Drever-Hall; SSB: single-side-band generator. The insert shows the used FFP resonator and one of its mirrors deposited on the ferule. (b) Superimposed square pump pulses measured with an optical sampling oscilloscope.

Bragg mirrors are deposited at each extremity with a physical vapor deposition technique, to achieve 99.84% reflectance over 100 nm [24] and obtain a resonator with a free spectral range (FSR) of 1.57 GHz for a finesse of $F = \pi\rho/(1-\rho^2) \approx 314$. To perfectly control the cavity detuning $\delta = -\phi_0$, we implemented a two-arms stabilization scheme in a similar way to [11] and [25]. The CW laser is split to obtain one beam for the stabilization (control beam) of the laser on a cavity resonance, and another one to pump the cavity (nonlinear beam). We adjust the polarization states of the control and nonlinear beams, with polarization controllers, in order to separate the beams with a polarization beam splitter at the output and also to make sure they do not interact with each other within the cavity. The stabilization [lower beige arm in the Fig. 2(a)] is performed thanks to a Pound-Drever-Hall system [26]. For the nonlinear beam [upper brown arm in Fig. 2(a)], we change the cavity phase thanks to a homemade tunable single-side-band generator [see SSB in Fig. 2(a)]. The nearest side band of a modulated beam, obtained with a phase modulator driven by a 30 GHz tunable frequency synthesizer, is isolated to obtain a pump signal with a tunable frequency shift. At the cavity output, we record the whole signal, corresponding to the steady states, and the new spectral component using a notch filter (fiber Bragg grating) to remove the pump component as in [9] [Fig. 3(e)]. In order to measure the characteristic phase values for which MI exists in the cavity [point 1, 2 and 3 in Fig. 1(a)], we scan a cavity resonance, by applying a

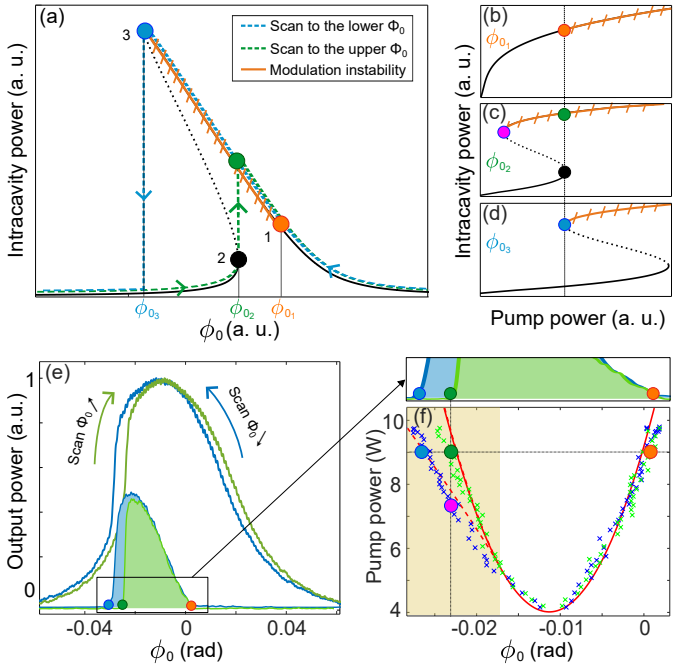

Fig. 3. (a), (b), (c) and (d) are theoretical explanations of the determination of the critical points, with the same numbering as Fig. 1. Black dotted lines represent unstable states. (e) and (f) are an example of experimental determination of the critical points for a pump duration $\delta t = 40$ ps. Colored circles are used to link the various figures, specifically to indicate the locations of critical points. (a) Nonlinear transfer function depending on the scan direction. Stationary states at different cavity phases, ϕ_{0_1}, ϕ_{0_2} and ϕ_{0_3}, respectively. The modulational unstable branch is pinpointed by the hatched orange lines. (e) Experimental scans, by increasing the phase (green) and decreasing the phase (blue), for $P_{in} = 9$ W. Solid lines: cavity output power; filled color plots: new spectral components obtained by removing the pump component of the output signal. (f) Delineation of the area where MI is observable. Crosses: experiments; red solid line: simulation by increasing the phase; red dashed line: simulation by decreasing the phase.

frequency sweep with the tunable frequency synthesizer, along one FSR of the cavity (between 30 GHz and 31.57 GHz) with a speed of 15.7 GHz.s^{-1} (i.e. 62.82 rad.s^{-1}). As the stabilization and nonlinear beams are almost independent, the scans are repeatable.

Figures 3(a), (b), (c) and (d) illustrate how we managed to measure the values of the characteristic points, by applying either positive or negative phase scans on the nonlinear beam. Starting from a high positive cavity linear phase (strong negative detuning) and by decreasing the phase, the system is initially monostable, reaches the bistable regime by following the upper branch [blue dashed line in Fig. 3(a)] and eventually jumps on the lower branch at the upper knee. Thus MI is observable between the MI threshold [orange circle in Fig. 3] and the upper knee [blue circle]. Conversely, starting form a high negative cavity linear phase (strong positive detuning) and by increasing the phase [green dashed line in Fig. 3(a)], the system is initially on the lower branch and jumps on the upper branch from the lower knee [black circle], at a different phase than for the previous scan, thus entering the system monostable regime. In this case, MI is triggered between the lower knee [black to green circle] till it reaches the MI threshold [orange circle in Fig. 3].

Fig. 3(e) presents the results of an ascending and descending phase scans for an input power of 9 W and a pulse duration of 40 ps. Note that, as mentioned above, all the power values mentioned refer to the peak power of the square-shaped pump pulses. The input peak power is determined by measuring the input average power P_{av}, using the expression $P_{in} = P_{av}/(FSR.\delta t)$, and checking the EDFA operates in a linear regime. The steady states [solid lines] and the new spectral components [filled colored plot] are superimposed to highlight the existence range of MI for both scans. As expected, the two scans do not provide the same results. By decreasing the phase [blue plots in Fig. 3(e)], we measure the MI threshold ($\phi_{0_1} = 0.001$ rad) [orange circle] and the upper knee position ($\phi_{0_3} = -0.026$ rad) [blue circle] by locating the edges of the range where the new spectral components due to MI appear. Note that at this point (blue circle) we observe the simultaneous jump to the lower branch of the steady state (blue line) and the fading of the MI spectral components (filled blue plot) as expected. In the same way, by increasing the phase [green plots in Fig. 3(e)], we measure the lower knee position ($\phi_{0_2} = -0.023$ rad) [green circle] and the MI threshold value (same point than the previous scan, orange circle). Again, at the green point we observe at the same time the steady state jump and the MI fading. By increasing the pump power from 0 to 10 W, and repeating the phase scans, we measured minimum and maximum phase values for which MI is observable [blue crosses in Fig. 3(f) for descending phase scans; green crosses for the ascending phase scans]. In the monostable region [white area in Fig. 3(f)], blue and green crosses overlap as they correspond to the MI threshold [orange circle]. In the bistable region [beige part in Fig. 3(f)], blue and the green crosses are distinct and constitute two separate branches. The upper one [green crosses] corresponds to the lower knee, and the lower one [blue crosses] to the upper knee. The experimental measurements are in perfect agreement with theoretical prediction [red line in Fig. 3(f)], obtained by locating the phase for which the gain [Eq.(2)] is positive when the system is monostable. For the bistable region, the red dashed line and the red solid line are obtained by locating the phase of the two knees [green and blue circles in Fig. 2(b), (c) and (d)]. As shown in Fig. 1, the coordinates (intracavity power and linear phase) of the three critical points depend on the pump duration. To evidence this dependence, we repeated the same experiment for durations ranging from 30 ps to 200 ps. For the sake of clarity, we focus on the MI threshold. Its evolution as a function of the pump pulse duration is represented

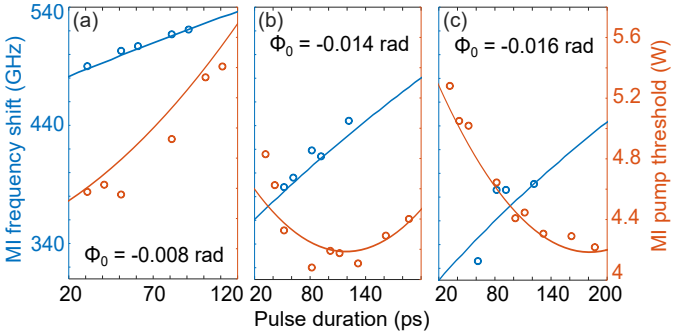

Fig. 4. MI threshold (orange) and frequency shift of the maximum MI gain (blue) as a function of the input pulse duration for a fixed phase. Circles: experiments; solid lines: numerics.

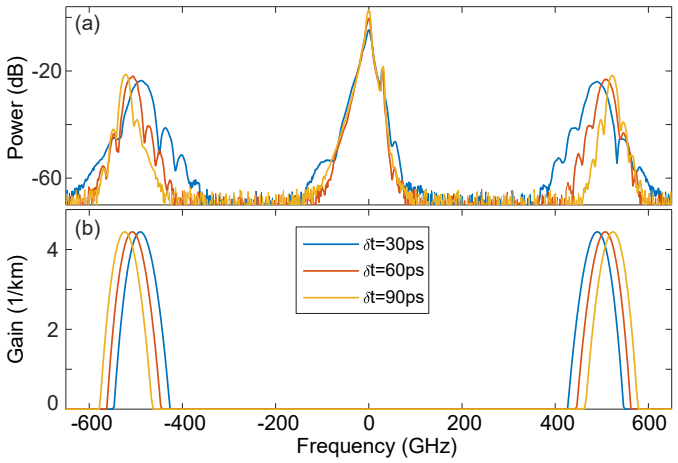

Fig. 5. MI lobes shift at the threshold as a function of the pulse duration, for $\phi_0 = -0.008$ rad. Blue line: δt = 30 ps; yellow line: δt = 60 ps; orange line: δt = 90 ps. (a) Experiment; (b) Theoretical gain spectrum

for three different phases, -0.008, -0.014 and -0.016 rad, respectively [orange circles in Fig. 4]. The experimental measurements [orange circles] are in good agreement with numerics [orange solid lines]. Depending on the phase value, MI threshold can significantly decrease or increase with the pump pulse duration. For instance, for a pulse duration variation of 170 ps, we observe a MI pump power threshold variation of more than 1.2 W. The orange curves in Fig. 4 show that the lower is the phase, the longer is the pump pulse corresponding to the minimum MI pump power threshold [23].

Another remarkable fact is the MI spectra dependence to the pump pulse duration. In [23], it is predicted that the MI gain lobes are shifted away from the pump by increasing the pump duration. Fig. 5(b) shows the evolution of the parametric gain, calculated with Eq.(2), for different pump durations at $\phi_0 = -0.008$ rad and a 64 W intracavity power (just above the MI threshold). The maximum of the MI gain lobes does not change with the pulse duration but they are frequency shifted. Corresponding experimental MI spectra shown in Fig. 5(a) have been recorded with a pump power just above the pump power threshold [orange plots in Fig. 4], i.e. $P_{90ps} = 5.3$ W, $P_{60ps} = 4.89$ W and $P_{30ps} = 4.57$ W, in a way that the intracavity power always remains the same (around 64 W). The MI side lobes are frequency shifted as the pulse duration is increased. The agreement with theoretical prediction is excellent. Note that the increase of the MI lobe width with decreasing pump duration in Fig. 5(a) is due to the spectra of the pump pulses themselves, wider for short pulses. To get a larger overview, we repeated these measurements for different pump durations, and report the results in Fig. 4 (blue circles). The MI frequency is shifted of more than 80 GHz for a pulse duration difference of 90 ps, in good agreement with theory.

In summary, we have investigated the impact of the pulse duration on modulation instability in FFP resonators. To quantify and clearly illustrate this phenomenon, we have studied the variation of three critical points: the MI threshold, the upper knee and the lower knee of the bistable region. We have shown that the pump power and the cavity phase of the MI threshold change with the pump duration. Moreover, we have shown that the pump duration modifies the MI side lobe position by decreasing the MI frequency shift at short duration. These experimental results are in good agreement with theory and confirm the importance of the contribution of the pulse duration in a pulsed pumping scheme of an FFP resonator. Our results contribute to a better understanding of the dynamics of Kerr comb generation in FFP resonators.

Funding. The present research was supported by the agence Nationale de la Recherche (Programme Investissements d'Avenir, I-SITE VERIFICO, FARCO, ASTRID ROLLMOPS); Ministry of Higher Education and Research; European Regional Development Fund (Photonics for Society P4S), the CNRS (IRP LAFONI); A.M.P. acknowledges support from The Royal Academy of Engineering through the Research Fellowship Scheme and from EPSRC Project EP/W002868/1; Hauts de France Council (GPEG project); and the university of Lille (LAI HOLISTIC)

Disclosures. The authors declare no conflicts of interest.

REFERENCES

1. T. Fortier and E. Baumann, Commun. Phys. **2**, 153 (2019).
2. T. J. Kippenberg, A. L. Gaeta, M. Lipson, and M. L. Gorodetsky, Science **361**, eaan8083 (2018).
3. A. Pasquazi, M. Peccianti, L. Razzari, D. J. Moss, S. Coen, M. Erkintalo, Y. K. Chembo, T. Hansson, S. Wabnitz, P. Del'Haye, X. Xue, A. M. Weiner, and R. Morandotti, Phys. Reports **729**, 1 (2018).
4. Y. Sun, J. Wu, M. Tan, X. Xu, Y. Li, R. Morandotti, A. Mitchell, and D. J. Moss, Adv. Opt. Photonics **15**, 86 (2023).
5. E. Obrzud, S. Lecomte, and T. Herr, Nat. Photonics **11**, 600 (2017).
6. K. Jia, X. Wang, D. Kwon, J. Wang, E. Tsao, H. Liu, X. Ni, J. Guo, M. Yang, X. Jiang, J. Kim, S.-n. Zhu, Z. Xie, and S.-W. Huang, Phys. Rev. Lett. **125**, 143902 (2020).
7. M. Nie, K. Jia, Y. Xie, S. Zhu, Z. Xie, and S.-W. Huang, Nat. Commun. **13**, 6395 (2022).
8. Z. Xiao, T. Li, M. Cai, H. Zhang, Y. Huang, C. Li, B. Yao, K. Wu, and J. Chen, Light. Sci. & Appl. **12**, 33 (2023).
9. T. Bunel, M. Conforti, Z. Ziani, J. Lumeau, A. Moreau, A. Fernandez, O. Llopis, J. Roul, A. M. Perego, K. K. Wong *et al.*, Opt. Lett. **48**, 275 (2023).
10. D. Braje, L. Hollberg, and S. Diddams, Phys. Rev. Lett. **102**, 193902 (2009).
11. Z. Li, Y. Xu, S. Shamailov, X. Wen, W. Wang, X. Wei, Z. Yang, S. Coen, S. G. Murdoch, and M. Erkintalo, Nat. Photonics (2023).
12. S. Coen and M. Erkintalo, Opt. Lett. **38**, 1790 (2013).
13. S. Coen and M. Haelterman, Phys. Rev. Lett. **79**, 4139 (1997).
14. S. Coen and M. Haelterman, Opt. Lett. **26**, 39 (2001).
15. A. Mussot, E. Louvergneaux, N. Akhmediev, F. Reynaud, L. Delage, and M. Taki, Phys. Rev. Lett. **101**, 113904 (2008).
16. M. Conforti, A. Mussot, A. Kudlinski, and S. Trillo, Opt. Lett. **39**, 4200 (2014).
17. F. Copie, M. Conforti, A. Kudlinski, A. Mussot, and S. Trillo, Phys. Rev. Lett. **116**, 143901 (2016).
18. P. Del'Haye, A. Schliesser, O. Arcizet, T. Wilken, R. Holzwarth, and T. J. Kippenberg, Nature **450**, 1214 (2007).
19. S. B. Papp, P. Del'Haye, and S. A. Diddams, Phys. Rev. X **3**, 031003 (2013).
20. M. H. Anderson, A. Tikan, A. Tusnin, J. Riemensberger, A. Davydova, R. N. Wang, and T. J. Kippenberg, Phys. Rev. X **13**, 011040 (2023).
21. W. J. Firth, J. B. Geddes, N. J. Karst, and G.-L. Oppo, Phys. Rev. A **103**, 023510 (2021).
22. D. C. Cole, A. Gatti, S. B. Papp, F. Prati, and L. Lugiato, Phys. Rev. A **98**, 013831 (2018).
23. Z. Ziani, T. Bunel, A. M. Perego, A. Mussot, and M. Conforti, arXiv (2023). ArXiv:2307.13488 [nlin, physics:physics].
24. J. Zideluns, F. Lemarchand, D. Arhilger, H. Hagedorn, and J. Lumeau, Opt. Express **29**, 33398 (2021).
25. K. Nishimoto, K. Minoshima, T. Yasui, and N. Kuse, Opt. Lett. **47**, 281 (2022).
26. R. W. P. Drever, J. L. Hall, F. V. Kowalski, J. Hough, G. M. Ford, A. J. Munley, and H. Ward, Appl. Phys. B Photophysics Laser Chem. **31**, 97 (1983).

FULL REFERENCES

1. T. Fortier and E. Baumann, "20 years of developments in optical frequency comb technology and applications," Commun. Phys. **2**, 153 (2019).
2. T. J. Kippenberg, A. L. Gaeta, M. Lipson, and M. L. Gorodetsky, "Dissipative Kerr solitons in optical microresonators," Science **361**, eaan8083 (2018).
3. A. Pasquazi, M. Peccianti, L. Razzari, D. J. Moss, S. Coen, M. Erkintalo, Y. K. Chembo, T. Hansson, S. Wabnitz, P. Del'Haye, X. Xue, A. M. Weiner, and R. Morandotti, "Micro-combs: A novel generation of optical sources," Phys. Reports **729**, 1–81 (2018).
4. Y. Sun, J. Wu, M. Tan, X. Xu, Y. Li, R. Morandotti, A. Mitchell, and D. J. Moss, "Applications of optical microcombs," Adv. Opt. Photonics **15**, 86 (2023).
5. E. Obrzud, S. Lecomte, and T. Herr, "Temporal solitons in microresonators driven by optical pulses," Nat. Photonics **11**, 600–607 (2017).
6. K. Jia, X. Wang, D. Kwon, J. Wang, E. Tsao, H. Liu, X. Ni, J. Guo, M. Yang, X. Jiang, J. Kim, S.-n. Zhu, Z. Xie, and S.-W. Huang, "Photonic Flywheel in a Monolithic Fiber Resonator," Phys. Rev. Lett. **125**, 143902 (2020).
7. M. Nie, K. Jia, Y. Xie, S. Zhu, Z. Xie, and S.-W. Huang, "Synthesized spatiotemporal mode-locking and photonic flywheel in multimode mesoresonators," Nat. Commun. **13**, 6395 (2022).
8. Z. Xiao, T. Li, M. Cai, H. Zhang, Y. Huang, C. Li, B. Yao, K. Wu, and J. Chen, "Near-zero-dispersion soliton and broadband modulational instability Kerr microcombs in anomalous dispersion," Light. Sci. & Appl. **12**, 33 (2023).
9. T. Bunel, M. Conforti, Z. Ziani, J. Lumeau, A. Moreau, A. Fernandez, O. Llopis, J. Roul, A. M. Perego, K. K. Wong *et al.*, "Observation of modulation instability kerr frequency combs in a fiber fabry–pérot resonator," Opt. Lett. **48**, 275–278 (2023).
10. D. Braje, L. Hollberg, and S. Diddams, "Brillouin-Enhanced Hyperparametric Generation of an Optical Frequency Comb in a Monolithic Highly Nonlinear Fiber Cavity Pumped by a cw Laser," Phys. Rev. Lett. **102**, 193902 (2009).
11. Z. Li, Y. Xu, S. Shamailov, X. Wen, W. Wang, X. Wei, Z. Yang, S. Coen, S. G. Murdoch, and M. Erkintalo, "Ultrashort dissipative Raman solitons in Kerr resonators driven with phase-coherent optical pulses," Nat. Photonics (2023).
12. S. Coen and M. Erkintalo, "Universal scaling laws of Kerr frequency combs," Opt. Lett. **38**, 1790 (2013).
13. S. Coen and M. Haelterman, "Modulational Instability Induced by Cavity Boundary Conditions in a Normally Dispersive Optical Fiber," Phys. Rev. Lett. **79**, 4139–4142 (1997).
14. S. Coen and M. Haelterman, "Continuous-wave ultrahigh-repetition-rate pulse-train generation through modulational instability in a passive fiber cavity," Opt. Lett. **26**, 39 (2001).
15. A. Mussot, E. Louvergneaux, N. Akhmediev, F. Reynaud, L. Delage, and M. Taki, "Optical Fiber Systems Are Convectively Unstable," Phys. Rev. Lett. **101**, 113904 (2008).
16. M. Conforti, A. Mussot, A. Kudlinski, and S. Trillo, "Modulational instability in dispersion oscillating fiber ring cavities," Opt. Lett. **39**, 4200 (2014).
17. F. Copie, M. Conforti, A. Kudlinski, A. Mussot, and S. Trillo, "Competing Turing and Faraday Instabilities in Longitudinally Modulated Passive Resonators," Phys. Rev. Lett. **116**, 143901 (2016).
18. P. Del'Haye, A. Schliesser, O. Arcizet, T. Wilken, R. Holzwarth, and T. J. Kippenberg, "Optical frequency comb generation from a monolithic microresonator," Nature **450**, 1214–1217 (2007).
19. S. B. Papp, P. Del'Haye, and S. A. Diddams, "Mechanical control of a microrod-resonator optical frequency comb," Phys. Rev. X **3**, 031003 (2013).
20. M. H. Anderson, A. Tikan, A. Tusnin, J. Riemensberger, A. Davydova, R. N. Wang, and T. J. Kippenberg, "Dissipative Solitons and Switching Waves in Dispersion-Modulated Kerr Cavities," Phys. Rev. X **13**, 011040 (2023).
21. W. J. Firth, J. B. Geddes, N. J. Karst, and G.-L. Oppo, "Analytic instability thresholds in folded Kerr resonators of arbitrary finesse," Phys. Rev. A **103**, 023510 (2021).
22. D. C. Cole, A. Gatti, S. B. Papp, F. Prati, and L. Lugiato, "Theory of Kerr frequency combs in Fabry-Perot resonators," Phys. Rev. A **98**, 013831 (2018).
23. Z. Ziani, T. Bunel, A. M. Perego, A. Mussot, and M. Conforti, "Theory of modulation instability in Kerr Fabry-Perot resonators beyond the mean field limit," arXiv (2023). ArXiv:2307.13488 [nlin, physics:physics].
24. J. Zideluns, F. Lemarchand, D. Arhilger, H. Hagedorn, and J. Lumeau, "Automated optical monitoring wavelength selection for thin-film filters," Opt. Express **29**, 33398 (2021).
25. K. Nishimoto, K. Minoshima, T. Yasui, and N. Kuse, "Thermal control of a Kerr microresonator soliton comb via an optical sideband," Opt. Lett. **47**, 281 (2022).
26. R. W. P. Drever, J. L. Hall, F. V. Kowalski, J. Hough, G. M. Ford, A. J. Munley, and H. Ward, "Laser phase and frequency stabilization using an optical resonator," Appl. Phys. B Photophysics Laser Chem. **31**, 97–105 (1983).